THE ASTROPHYSICAL JOURNAL, 446:155–166, 1995 June 10

HST IMAGING POLARIMETRY OF NGC 1068[1]

A. CAPETTI,[2] D. J. AXON,[2,3] F. MACCHETTO,[2,3] W. B. SPARKS,[2] AND A. BOKSENBERG[4]
Received 1994 July 5; accepted 1994 December 16

ABSTRACT

We present the results of high-quality pre-refurbishment *HST* imaging polarimetry of NGC 1068 obtained with the Faint Object Camera in the ultraviolet ($\lambda \sim 2700$–3700 Å), and the Wide Field Planetary Camera in the visual ($\lambda \sim 5000$–6000 Å), with resolutions of 0".06 and 0".08, respectively.

The polarization of the UV continuum is very high, peaking at ~60% in the vicinity of the emission line knot 4".5 NE of the nucleus.

To a high degree of precision the polarization vectors show the centro-symmetric pattern expected from scattering from a point source. By locating the centre of symmetry of this pattern we have determined the location of the hidden nuclear source, to an accuracy of ±0".05, which lies 0".6 south of the emission peak.

A pair of highly polarized clouds ($P \sim 45\%$ in the UV) lies close to the position of the scattered nuclear source. The degree of polarization after correction for dilution is close to 100%, indicating that this is a reflection image. These clouds are associated with the "twin-crescent" object, a ringlike or double-jet like feature. Their peculiar properties suggests that they are related to the hidden nucleus. They probably represent reflection clouds produced by an expanding bipolar structure, or a jet. The hidden nucleus would lie at its center.

The WF/PC-I polarization images contain contributions from both optical continuum and emission lines. However, these two components are spatially separated. The continuum polarization dominates in a quasi-linear region starting at the location of the "hidden nucleus" and including the continuum peak, knot B. The nature of this pattern suggest that the nuclear light might be collimated. The large-scale polarization structure is dominated by scattered line emission. The source of this scattered [O III] emission is predominantly the bright observed region of line emission in the NLR, knot B. Therefore, scattering is also very important for narrow lines and this must be taken into account when trying to understand the kinematics and morphology of the NLR.

The nuclear radiation cone is only partly filled with scatterers; the minimum angular extent is from PA −15 to PA +55, corresponding to an opening angle greater than 70°, but it is probably as large as 100°.

It is difficult to establish the precise association between radio and optical emission because of the relatives errors between the respective reference frames. Adopting the registration of Evans et al. leads to the conclusion that there is no significant radio emission from the nucleus. This maybe because the radio nucleus is radio quiet, or, as both the theoretical model of the torus and the X-ray data imply, the column density in front of the nucleus is sufficient that free-free absorption obscures it even at centimeter wavelengths. Alternatively, if the flat spectrum southern radio component is assumed to be the nucleus, then there appears to be no direct spatial correspondence between the radio and the emission line structures.

Subject headings: galaxies: individual (NGC 1068) — galaxies: Seyfert — polarization — ultraviolet: galaxies

1. INTRODUCTION

Since the discovery of significant optical polarization in Seyfert nuclei (Walker 1968; Visvanathan & Oke 1968) the study of their polarized flux has proved to be a powerful tool for probing the geometry of their inner regions. Optical spectropolarimetry first provided evidence that scattering was important in the continuum on Seyfert 2 galaxies (Angel et al. 1976; Schmidt & Miller 1985) even though the observed polarization was severely diluted by starlight (McLean et al. 1983). The most significant results obtained from such observations has been the discovery that the polarized spectrum of many Seyfert 2 reproduces the spectrum of a Seyfert 1 showing broad Balmer lines and strong [Fe II] emission (Antonucci 1993; Axon et al. 1994, and references therein). The implication of this discovery is that these Seyfert 2 galaxies contain a Seyfert 1 nucleus whose BLR is occulted in our direct line of sight but which can be seen in reflection from scatterers surrounding the obscuring material.

Moreover, this suggests a unification scheme for Seyfert galaxies in which an optically thick torus surrounds the nuclear source: depending on the torus orientation the observer can have a direct view of the nucleus and of the broad line region (Seyfert 1) or these can be obscured and only the NLR will be observable (Seyfert 2).

NGC 1068 is the brightest and nearest classical Seyfert 2 and was the first object in which such scattered broad lines were discovered (Miller & Antonucci 1983; Antonucci & Miller 1985). The high spatial resolution attainable with the *HST* offers a unique possibility to resolve the detailed structure of its nuclear regions.

A fundamental question is the location of the hidden nucleus of NGC 1068 with respect to the reflecting screen and to the

[1] Based on observations with the NASA/ESA *Hubble Space Telescope*, obtained at the Space Telescope Science Institute, which is operated by AURA, Inc., under NASA contract NAS 5-26555 and by STScI grant GO-3594.01-91A.

[2] Space Telescope Science Institute; 3700, San Martin Drive, Baltimore, MD 21218.

[3] Astrophysics Division, Space Science Department of ESA; Estec, NL-2200 AG Noordwijk, The Netherlands.

[4] Royal Greenwich Observatory; Madingley Road, Cambridge CB3 0EZ, UK.

emission-line region. To date observations at different wavelengths and resolution (see for example Braatz et al. 1993) have not been able to provide a clear cut answer to this problem.

A second major issue is the nature and the origin of the particles responsible for the scattering of the nuclear light. In NGC 1068, the polarization level is found to be independent of wavelength in the optical and ultraviolet, when allowance is made for the dilution (Antonucci & Miller 1985; Code et al. 1993); this suggests that free electrons are responsible for the scattering. X-ray observations (Marshall et al. 1993) lead to the same conclusion. The free electrons can be associated with a hot outflowing wind (Krolik & Vrtilek 1984). However this inference depends critically on the large dilution correction and on the basis of the optical data alone Bailey et al. (1988) concluded that it is possible to account for the polarization in terms of dust processes. More rigorous attempts to model the UV to IR polarized flux spectrum of NGC 1068 (Young et al. 1995) point more clearly to electron scattering as the primary polarization mechanism at short wavelengths, but require a significant dichroic contribution from aligned grains in the torus to explain the near IR properties of the nucleus.

As part of a program to investigate the nature of nearby AGNs, we have carried out imaging polarization observations of NGC 1068 in both the UV with the FOC and used archival data obtained in the visible with WF/PC-I. The results, which we present here, not only resolve the issue of the location of the nucleus, but also allow us to explain several of the more puzzling features of the continuum and emission line polarization morphologies and polarization properties which have been measured with previous *HST* (Antonucci, Hurt, & Miller 1994; Caganoff et al. 1991) and ground-based observations (Bailey et al. 1988; Miller, Goodrich, & Mathews 1991; Inglis et al. 1995).

The paper is structured as follows. Details of the observations and the data reduction process are given in § 2; the reliability of the polarization observations taken with *HST* is assessed in § 3, while the results themselves are presented in § 4. In § 5 we derive the location of the active nucleus and in § 6 we discuss the polarization properties of the peculiar "twin-crescent" structure. The origin of the optical polarization is analyzed in § 7 and the distribution of gas and scatterers in § 8. The relationship between radio and optical images is examined in § 9. The discussion of these results is in § 10. In § 11 we give a summary.

Throughout this paper $H_0 = 50$ km s^{-1} Mpc^{-1} is adopted. Given its redshift of $z = 0.0038$, NGC 1068 is at a distance of 22.7 h_{50}^{-1} Mpc, where 0".1 corresponds to 11 h_{50}^{-1} pc.

2. OBSERVATIONS AND DATA REDUCTION

NGC 1068 was observed using the Faint Object Camera (FOC) and the Wide Field Planetary Camera (WF/PC-I) on board the *Hubble Space Telescope*.

2.1. *The FOC Observations*

FOC observations were obtained in 1993 September 30, in the f/96, 512 × 512 mode (Paresce 1992); the pixel size is 0".022 × 0".022 and the field of view about 11" × 11". We used the three different polarizer filters (POL0, POL60, and POL120) in combination with the wide ultraviolet filter F320W. Two exposures of 1800 s duration were made for each of the polarizers.

The data were processed to correct for geometric distortion using the grid of regularly spaced reseau marks on the faceplate of the detector; the data frames were then divided by normalized and geometrically corrected internal flat-field frames. The reseau marks were removed from the images with values taken from neighboring pixels. Flat-field linearity correction was applied (Jedrzejewski 1992). The peak of emission is saturated in our observations. Non linearity in FOC images is associated with a low-level noise which was removed by Fourier filtering.

All the images were deconvolved using 40 iterations of Lucy's (1974) algorithm and point spread functions were derived from the observations of the standard star BPM 16274 through the F320W filter; no PSF taken with the polarizer filters is available.

The polarizers are known to produce a displacement in the output images, with small but significant differences from filter to filter (Hodge 1993). The registration of the images has been performed in two ways, using the cross-correlation method and the positions of five point sources that are present in the FOC field of view. The two methods agree to within about 0.2 pixels. From the profile of the point sources we derive a resolution FWHM of 0".06 after the deconvolution.

The deconvolved and aligned images have been combined to produce maps of the Stokes parameters I, Q, and U:

$$I = \tfrac{2}{3}(I_0 + I_{60} + I_{120}),$$

$$Q = \tfrac{2}{3}(2I_0 - I_{60} - I_{120}),$$

$$U = \frac{2}{\sqrt{3}}(I_{60} - I_{120}),$$

and of polarized flux $I_P = (Q^2 + U^2)^{1/2}$, percentage of polarization $P = I_P/I$ and position angle $\theta = 0.5 \tan^{-1}(U/Q)$.

The statistical errors in the Stokes parameters were computed assuming Poisson noise in the images, and ignoring cross terms in the covariance matrix. The errors on the degree and position angle of the polarization are then estimated as

$$\sigma_P = \sqrt{2} N^{-1/2}$$

$$\sigma_\theta = \sqrt{2} N^{-1/2} P^{-1},$$

where N are the total counts in the component.

The data were debiased using the correction of Wardle & Kronberg (1974)

$$I_P = I_{P_{\rm obs}} \left(1 - \frac{\sigma_{I_P}}{I_{P_{\rm obs}}}\right)^{1/2},$$

where P and $P_{\rm obs}$ are the corrected and observed polarization flux and σ_P is the noise in the polarization image. As we describe below the good agreement between our results and those obtained by previous authors at lower spatial resolution indicates that our treatment of the data is reliable.

2.2. *The WF/PC-I Observations*

The WF/PC-I observations were taken in 1992 January 5, in the PC mode, with a pixel size of 0".043 × 0".043. The four 800 × 800 pixels CCD cover a field of view of 66" × 66". Three different polarizers were used in combination with the F555W filter and double exposures of 400 seconds were taken in each case. The data were processed by the WF/PC-I Science Data Processing pipeline performing the following operations: bias level removal, bias image subtraction, preflash image scaling and subtraction, dark image scaling and subtraction and flat-field image correction (MacKenty et al. 1992).

Individual exposures were combined to remove cosmic rays and the resulting images were then deconvolved using 50 iter-

ations of the Lucy's (1974) algorithm. The registration was performed by both cross-correlating the different images and by using the position of the point sources of the field. The resolution estimated from the profile of the point sources after the deconvolution is 0".08 FWHM. The images have been scaled as suggested by the results of the calibration observations (see § 3.2). Finally, the deconvolved and aligned images were combined to produce the polarization maps in the same way as for the FOC data.

3. THE POLARIZATION CALIBRATION

Before presenting the results, it is important to discuss the calibration of the *HST* polarization observations. We can use both calibration observations and previous ground-based polarization observations of NGC 1068 in order to assess the quality of our data.

3.1. *The FOC Data*

3.1.1. *Systematic Errors*

Two effects can produce systematic errors in the FOC polarization measurements: differences in the transmission curve of the polarizers and residual transmittance in the direction perpendicular to the plane of polarization of the filter.

Figure 1*a* compares the overall absolute quantum efficiency appropriate for the observations with the POL0 and POL60 polarizers. There are minor deviations between the two curves; they correspond to a 0.9% count rate difference (the POL0 flux tend to be overestimated) for a flat and unpolarized incident spectrum. However, in the wavelength region above 3000 Å, where most of the flux is expected, they produce a difference in the count rate of 0.6%. In the same region the POL0 and POL120 polarizers (Fig. 1*b*) also differ by 0.6%.

In the range 2700–3700 Å the FOC polarizers have a minor to principal transmittance of ~1% for POL60 and POL120 and ~0.5% for POL0. The first effect produces a systematic error of less than $\sigma_\theta \sim 0.4$ degrees on the polarization angle; the second leads to a systematic underestimate of the degree of polarization, ~0.1% on a 10% polarization level, and to $\sigma_\theta \sim$ 0.3 degrees. Moreover the errors on the polarization angle arising from these two effects tend to cancel each other because they are of opposite sign.

3.1.2. *Saturation, Deconvolution, and Registration*

The peak of the emission is saturated in our observations; therefore the halo of the PSF cannot be effectively removed by the deconvolution process. This is likely to alter the low brightness structure around the nucleus. To be certain that our analysis is not affected by this problem, we therefore limit ourselves to the study of the high brightness structures. Within the inner 5" of the field of view, polarization images were computed where the polarization and the total intensity map have a signal-to-noise ratio greater than 20 and 200, respectively. Outside this inner region, the saturation effects are negligible and therefore the fainter structure could also be analyzed.

The spatial registration is estimated to be accurate to within 0.2 pixels. The effects of mis-registration have been tested by shifting the images by 0.3 pixels with respect to the optimum alignment. The fractional polarization changes an average of about 0.03 (e.g. 0.3% rms on a 10% polarization level) and the polarization angle changes by about 0°.8. In regions of strong intensity gradients these values are higher, up to 0.20 and 5°, respectively.

3.1.3. *Comparison with Previous Observations of NGC 1068*

From the Wisconsin Ultraviolet Photo Polarimeter Experiment (WUPPE) Code et al. (1993) obtained ultraviolet spectro-

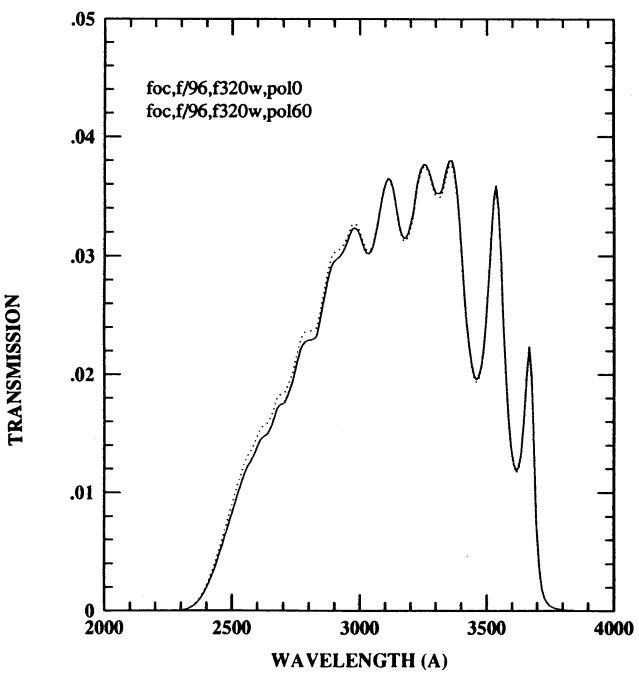

FIG. 1*a*

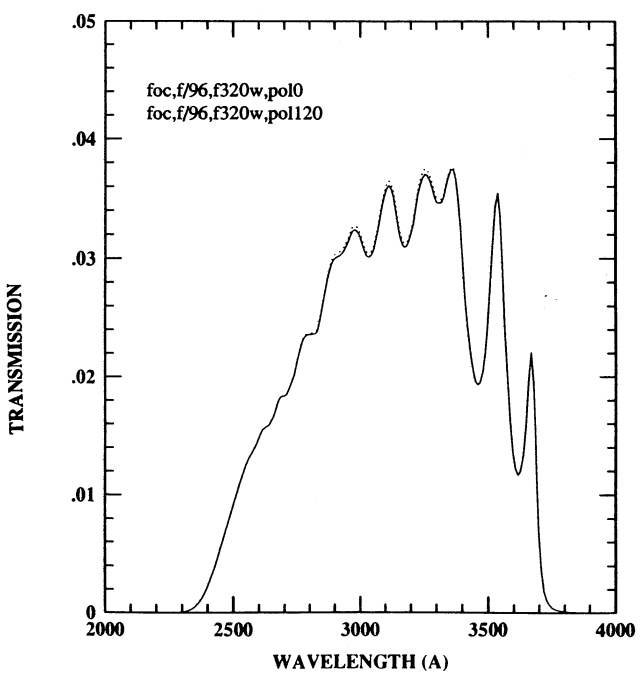

FIG. 1*b*

FIG. 1.—(*a*) Comparison of the overall absolute quantum efficiency for the POL0 + F320W (*dotted line*) and POL60 + F320W (*solid line*); (*b*) comparison of the POL0 + F320W (*dotted line*) and POL120 + F320W (*solid line*).

polarimetry of NGC 1068; through an aperture 6″ × 12″ they measured an average polarization $P = 12.9\% \pm 1.9\%$ at a position angle of $\theta = 112.^{\circ}0 \pm 3.^{\circ}8$ in the wavelength range 2500–3200 Å. By producing a synthetic aperture on the FOC data, whose size and orientation match as closely as possible that of WUPPE we find a polarization of $14.5\% \pm 0.6\%$ at a position angle of $111.^{\circ}6 \pm 1.^{\circ}2$. The ground-based observations of Miller & Antonucci (1983) through a 2″.8 circular aperture centered on the nucleus at 3700 Å gave $P = 8.0\%$ and $\theta = 96°$. Again synthesizing their aperture on the FOC data we obtain $P = 9.4\% \pm 0.1\%$ at a position angle of $\theta = 97.^{\circ}5 \pm 0.^{\circ}2$. As a final check, we carried out the same procedure for the northeast polarized knot, Miller et al. (1991) found $P \sim 30\%$ and $\theta \approx 125°$ at 3500 Å and we measure $P = 31.1\% \pm 0.5\%$ and $\theta = 125.^{\circ}1 \pm 0.^{\circ}8$.

The very good agreement between our results and those previously published, particularly in polarization angle, demonstrate the integrity of the UV data, and our treatment of it described in § 2, even though it was obtained prior to the installation of COSTAR.

3.2. *The WF/PC-I Data*

3.2.1. *Calibration Observations*

Calibration observations of polarized and unpolarized standard fields have been taken for the WF/PC-I as part of the STScI calibration program. Observations of the unpolarized standard star GD 319 have been used to compare the transmission of the three polarizers combined with the F555W filter. The transmission of the POL60 and POL120 filters differs from the POL0 filter by −5.5% and +3.3%, respectively. This correction has been applied to observations of the reflection nebula R Mon; the resulting polarization pattern, degraded to 1″ resolution, is presented in Figure 2 and shows the centrosymmetric pattern already known from ground-based observations (e.g., Scarrott, Draper, & Warren-Smith 1989). The standard polarized field RMON3 has a polarization of $P = 11.9\%$ at a position angle of $\theta = 87.7$ (Turnshek et al. 1990); we found $P = 9.5\%$ and $\theta = 94.4$. We ascribe this difference in measured values of P to a combination of the uncertainties in the location of the Turnshek aperture and variability of the source. In terms of the analysis presented in this paper the most important aspect of this result is the good agreement in position angles.

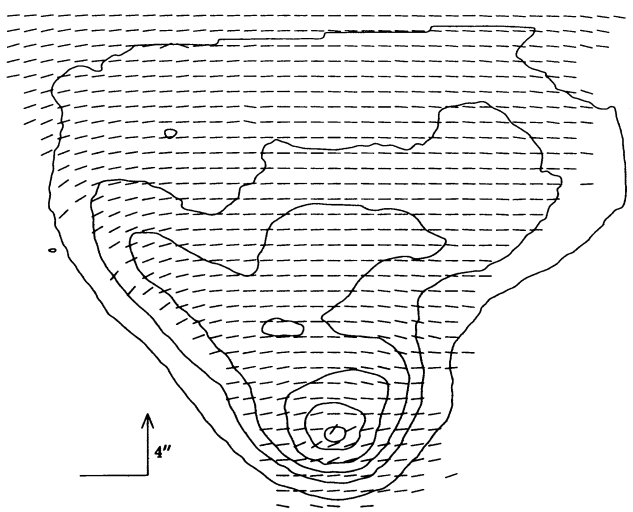

FIG. 2.—Polarization vectors of the reflection nebula R-Mon, used for the calibration of the WF/PC-I polarization observations, superposed to the total intensity contours. The images have been degraded to 1″ resolution.

3.2.2. *Comparison with Previous Observations of NGC 1068*

The WF/PC-I data can be compared with the observations of Scarrott et al. (1991) who obtained a polarization map from V band observations. Through a simulated 1″.6 aperture they found $P = 2.52\% \pm 0.5\%$ and $\theta = 102.^{\circ}9 \pm 2.^{\circ}9$. However, unlike the V filter, the F555W filter also includes the prominent oxygen lines [O III] λλ4959,5007. The forbidden emission lines have a different position angle and a lower polarization with respect to the continuum (Bailey et al. 1988); for the [O III] λ5007 line they found $P = 1.10\% \pm 0.02\%$ and $\theta = 142.^{\circ}0 \pm 0.^{\circ}5$ through a 2″.8 aperture centered on the nucleus.

Using the same simulated aperture of Scarrott et al. we find $P = 1.9\% \pm 0.1\%$ and $\theta = 121° \pm 4°$; in this case the errors quoted are dominated by the uncertainties in positioning their aperture on our images.

This result can be easily understood since we are observing a combination of line and continuum emission leading to polarization parameters intermediate between those of the two components. Since the equivalent width in the polarized flux of the [O III] lines is similar to the width of the F555W filter (∼1000 Å), there is an equal contribution to the polarized flux of line and continuum emission; in this case we expect to find $P = 1.8\%$ and $\theta = 122°$ in good agreement with our observations.

Inglis et al. (1995) carried out ground-based spectropolarimetric observations of NGC 1068 at different locations outside the nucleus with a 1″.3 × 2″.7 aperture; placing this aperture in our images at 2″.5, 5″.0, and 7″.5 northeast of the nucleus, the same locations of Inglis et al., we find that our position angle is in agreement (to within 5°) with their measurement of the position angle of the [O III] lines.

The effect of mis-registration are stronger than for the FOC images. For a shift of 0.1 pixels, the fractional polarization changes on average of about 0.08 and the polarization angle of 2.°8.

We conclude that polarization measurements from the WF/PC-I data are also reasonably accurate, with a typical error in polarization angle not exceeding 5°.

4. RESULTS

4.1. *The Ultraviolet Polarization*

The polarization image (Fig. 3 [Pl. 1]) is dominated by a small number of resolved clouds which follow closely the structure of the total intensity image. In the region of higher brightness the data is saturated and the image has been masked. Toward the northeast the extended emission is filamentary. The polarization structure is highly asymmetrical, with most of the emission concentrated in the northern lobe, while the southern lobe is barely detected.

The image of percentage of polarization (Fig. 4 [Pl. 2]) shows values as high as 60%. These are much higher than has been reported previously which indicates that there is a considerable dilution in the ground based apertures. In these regions most of the observed light is reflected. There is an abrupt division in this image: close to the nucleus the percentage of polarization is typically 8%–15% but for distances greater than ∼3″ from the nucleus the polarization is much higher, ranging from 20% up to 60%. A major exception is a pair of highly polarized clouds seen 0″.6 south of the emission

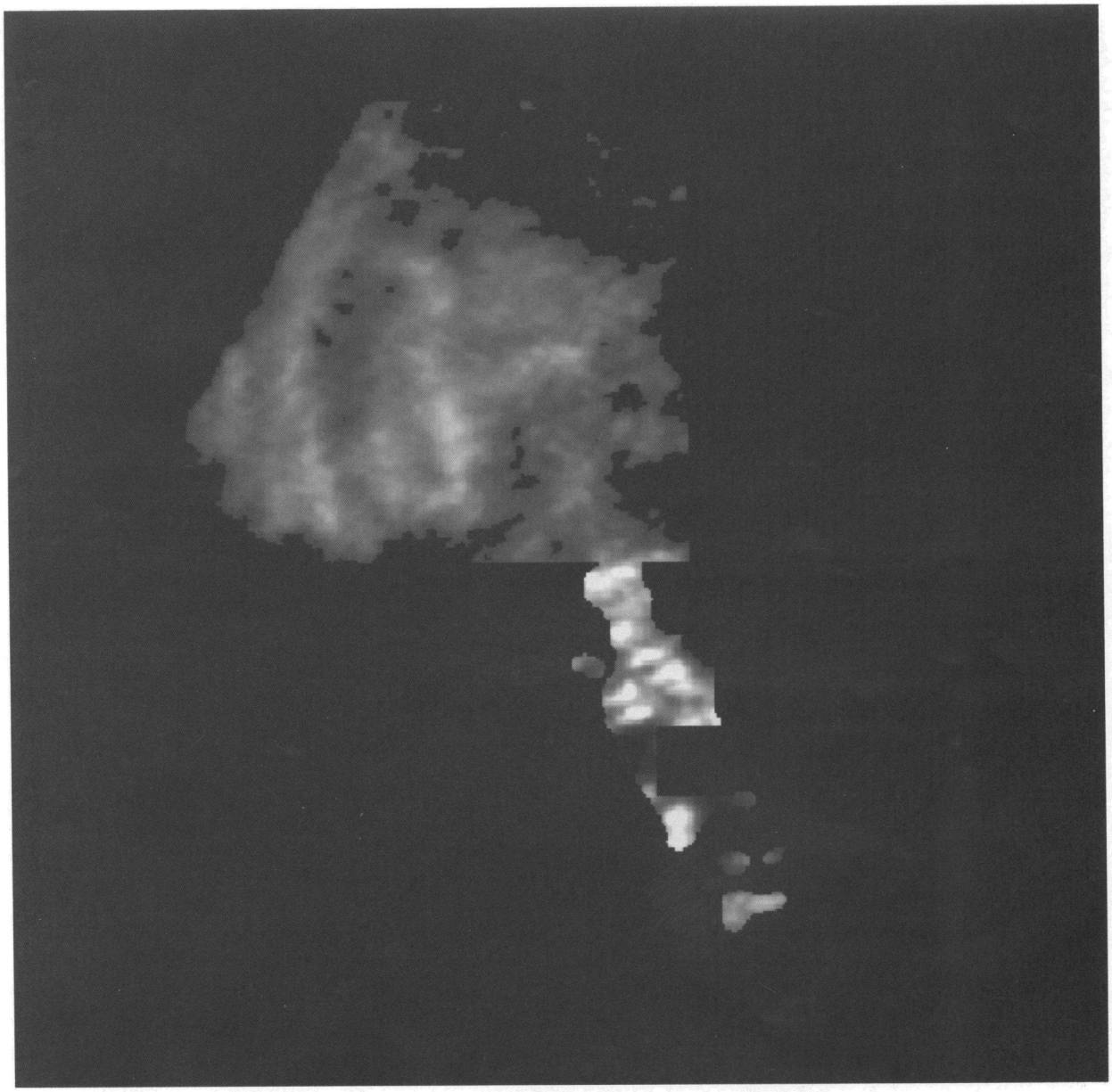

FIG. 3.—Polarized flux map from the FOC observations. The field of view is 9″ × 9″. North is at the top, east is to the left. All the images are presented in the same orientation.

CAPETTI et al. (see 446, 158)

PLATE 2

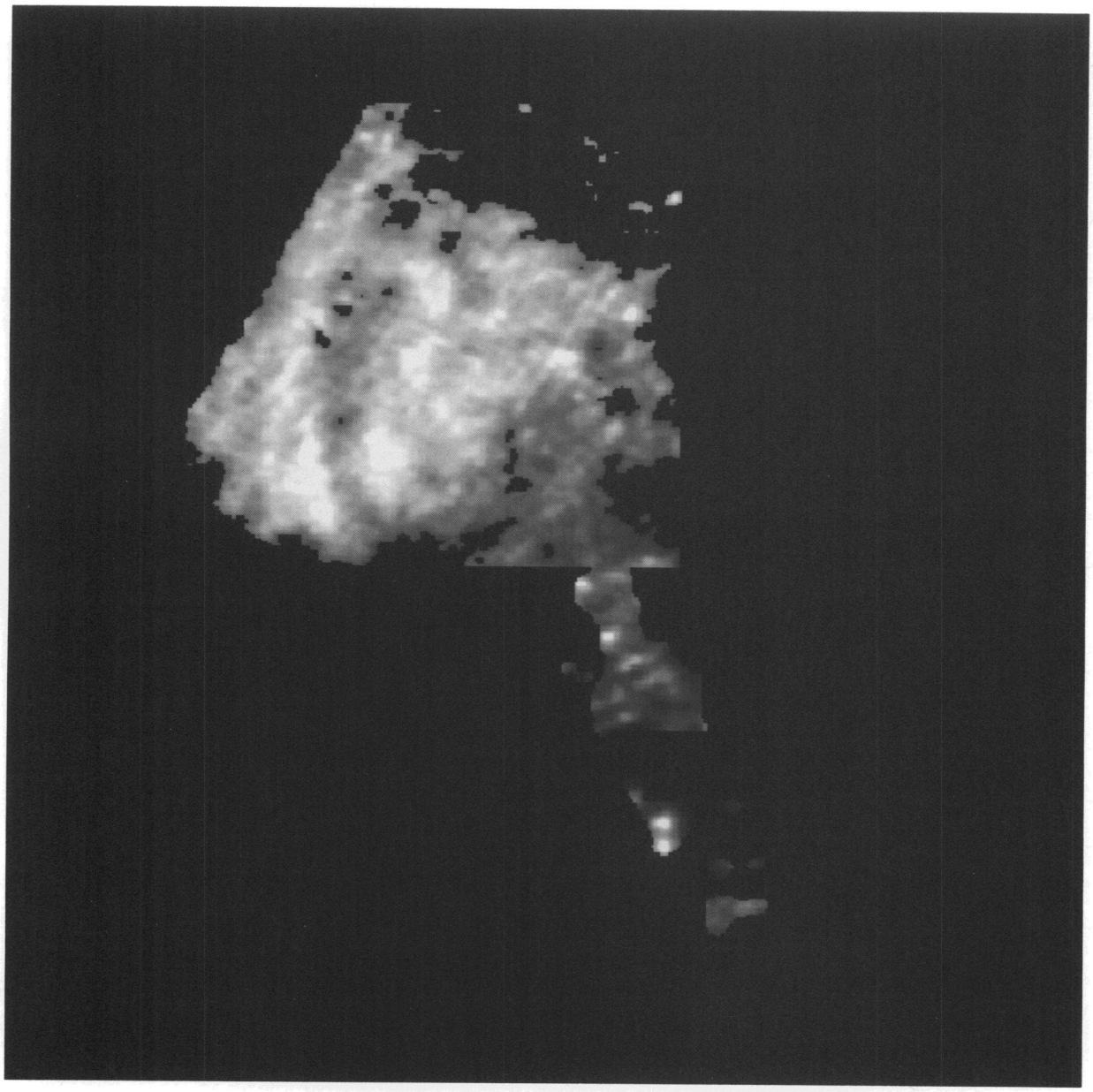

FIG. 4.—Map of degree of polarization from the FOC observations

CAPETTI et al. (see 446, 158)

peak. They clearly stand out in the image of percentage of polarization where they reach 50% polarization.

Figure 5 shows the polarization vectors derived from the FOC images. The reader is cautioned that these have been plotted with a fixed length so that the geometrical pattern they form is clear at all radii. The polarization pattern is very regular; to a high degree of precision the polarization vectors show a centro-symmetric pattern around the position of the source of the scattered radiation.

4.2. *The Visual Polarization*

Figure 6 (Plate 3) shows the total intensity map (the Stokes parameter *I*) obtained from the WF/PC-I observations. It is dominated by an extended bright cloud which coincides with the peak of continuum emission seen by Lynds et al. (1991). Two smaller bright regions can be seen toward the northeast. The lower-brightness emision, even if less prominent than in the FOC images, still outlines the overall conical shape. The galaxy starlight is also apparent in this image.

The structure seen in the polarization image (Fig. 7 [Pl. 4]) is quite different from the image of total intensity; the three brightest clouds in total intensity correspond to the brightest region even in the polarized image. However, one region of high polarization appears toward the South; its position is coincident with the pair of high polarization clouds detected in the FOC images. The high polarization region toward the northeast of the nucleus can also be seen in Figure 7. Moreover regions of polarized flux can be found toward the east and the southwest of the brightest regions.

These features are also evident in the image of percentage of polarization, smoothed at 0.″2 resolution, shown in Figure 8 (Plate 5). The degree of polarization is quite small everywhere, typically ~2%–4%, but in the northeast region and in the south polarized region can be as high as 15%. The masked area in Figures 7 and 8 is due to a region of unreliable flat field.

Figure 9 plots the polarization vectors (again with a fixed length) obtained from the WF/PC-I observations in the innermost 3″. The polarization pattern is more complex than the simple centro symmetric structure observed in the FOC images. It shows two different components. One component is oriented at PA ~90°; it has a linear structure and includes the South polarized region and the two western brightest blobs. The second component is polarized at PA ~135° and covers most of the extended polarized emission.

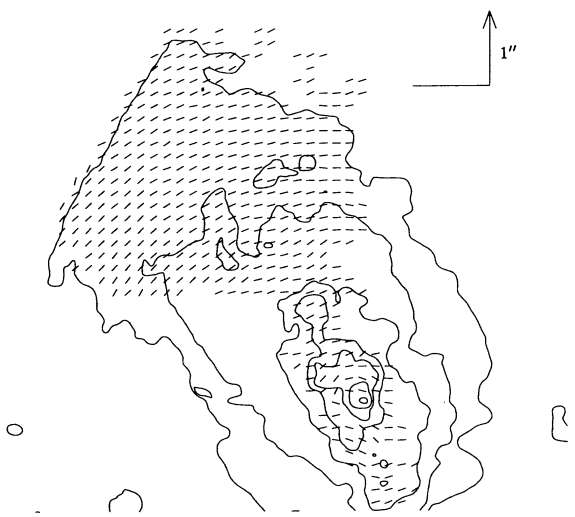

FIG. 5.—Polarization vectors from the FOC observations. To show more clearly the polarization pattern, the length of the vectors is constant and not proportional to the polarization level. Superposed we show the total intensity contours.

FIG. 9.—Polarization vectors from the WF/PC-I observations. To show more clearly the polarization pattern, the length of the vectors is constant and not proportional to the polarization level. Superposed we show the total intensity contours.

Figure 10 plots the polarization vectors on a larger scale, 10″. The polarized flux extends much farther toward the NE and the SW, at PA ~135°. A third, weaker component, appears on the East side of the nucleus with polarization angle ~45°.

5. LOCATION OF THE HIDDEN NUCLEUS

The pattern of the UV polarization vectors can be used to derive the position of the active nucleus; in fact, the radius vector from the nucleus to any point in the image is perpendicular to the polarization vector. We determined the location of the nucleus that best reproduces the polarization pattern observed; the uncertainty on the position of the nucleus

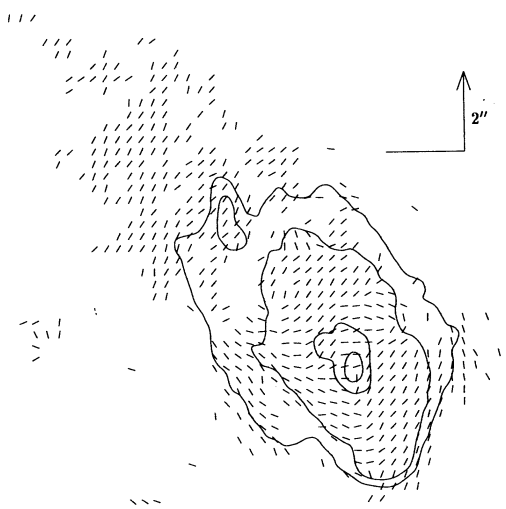

FIG. 10.—Large-scale polarization vectors from the WF/PC-I observations. Superposed we show the total intensity contours.

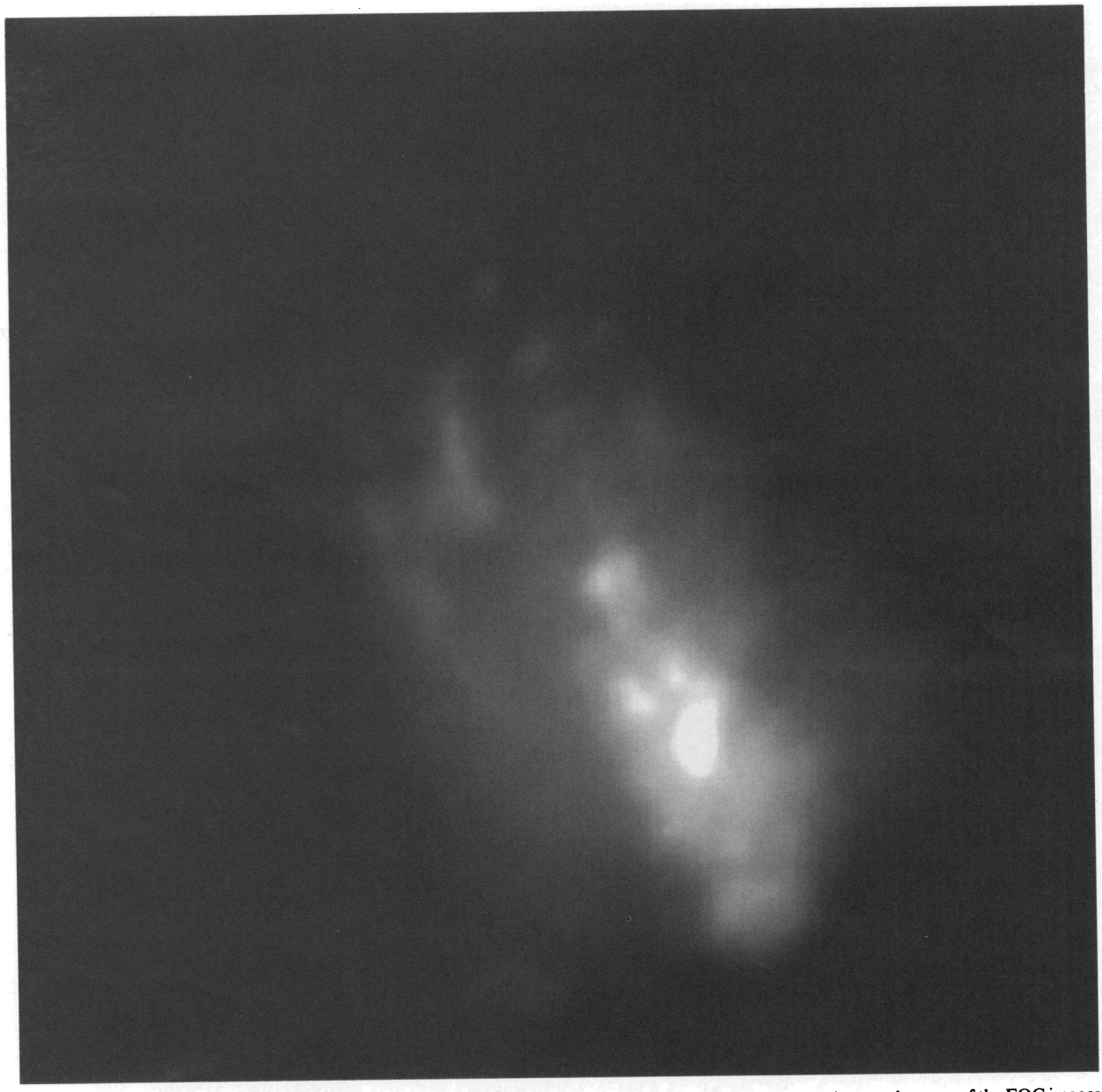

FIG. 6.—Total intensity map (the Stokes parameter *I*) from the WF/PC-I observations; field of view and orientation are the same of the FOC images, 9″ × 9″

CAPETTI et al. (see 446, 159)

PLATE 4

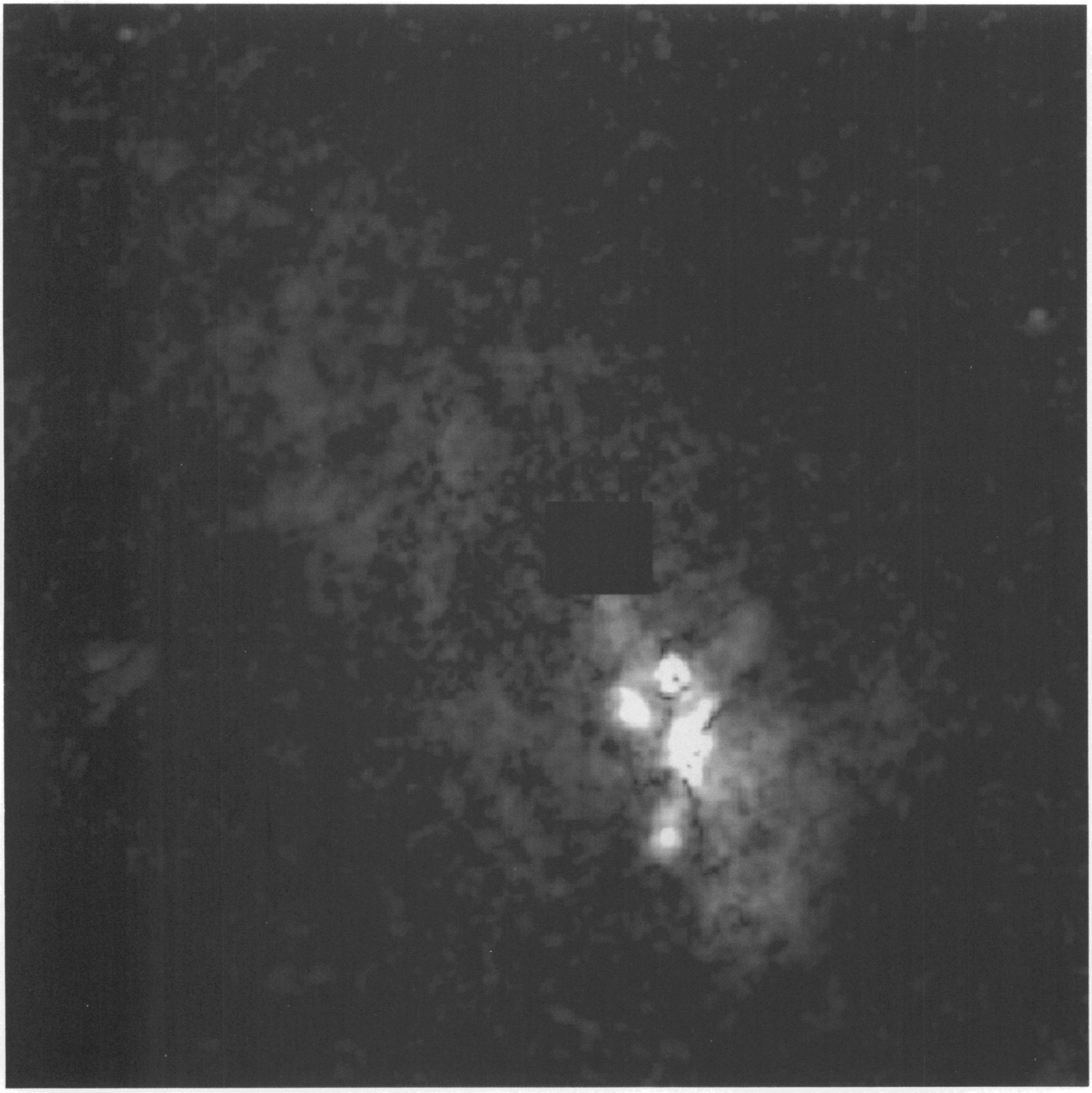

FIG. 7.—Polarized flux map from the WF/PC-I observations. The masked area is due to a region of unreliable flat-field.

CAPETTI et al. (see 446, 159)

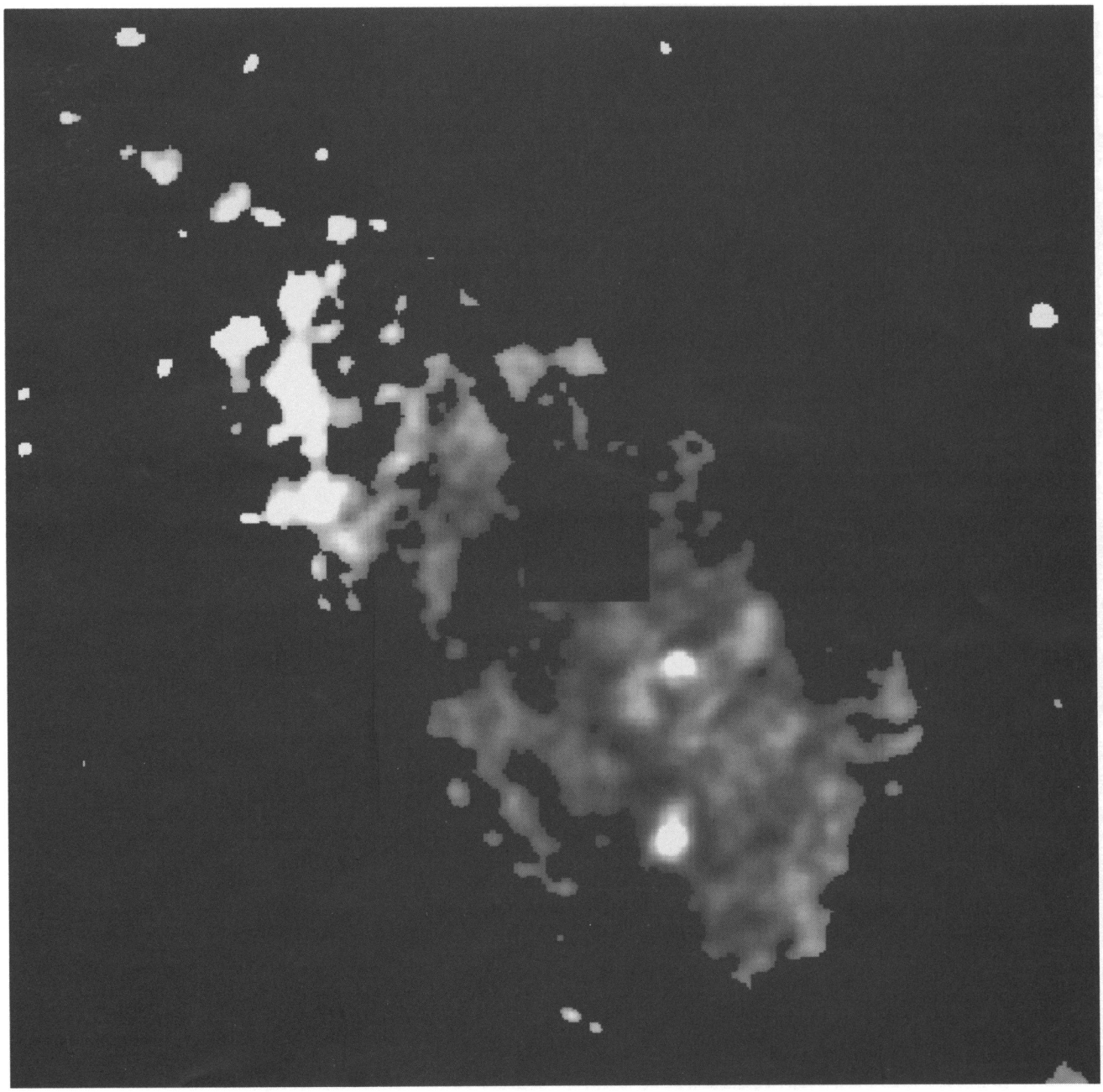

FIG. 8.—Map of degree of polarization from the WF/PC-I observations smoothed at 0".2 resolution. The masked area is due to a region of unreliable flat field.

CAPETTI et al. (see 446, 159)

obtained with this procedure is ± 2 pixels, corresponding to less than 0".05. The effect of a systematic error corresponding to $\pm 2°$ on the polarization angle, well within our estimate, is to shift the position of the nucleus by $\sim 0".1$ in the EW direction.

This procedure implicitly assumes that the nucleus is an unpolarized point source. If the nucleus is polarized, significant deviations of the polarization vectors with respect to a perfect circular pattern are expected. Figure 11 plots these deviations; each point represents the average of all the points along a particular position angle from the nucleus. Using the χ^2 goodness of fit test, the residuals distribution is consistent with a null average deviation at the 99% confidence level.

If the nucleus was not a point source the pattern of the polarization vectors would no longer be circular. The polarization angle θ' produced by scattering of a source of given radius a is (see Fig. 12)

$$\tan \theta' = \tan \theta \cdot \left[1 - \frac{a(r_2 + r_1)}{x_0(r_2 - r_1)}\right]^{-1},$$

where θ is the polarization angle for a pointlike source. The dotted line in Figure 11 shows the pattern obtained for $a = 0".3$. Therefore, the estimate of the position of the nucleus is largely independent on its actual light distribution and the point source approximation is very accurate.

The presence of emission lines within the spectral range of the F320W filter (e.g., Mg II λ2800, O III λ3130, [Ne V] λ3426) can also lead to an error in the position of the nuclear source; in fact the emission lines are polarized at a different position angle with respect to the featureless continuum. The error in determining the continuum position angle is given by

$$\Delta\theta = \frac{\epsilon \cdot \sin(\theta_c - \theta_l)}{1 + \epsilon \cdot \cos(\theta_c - \theta_l)} \quad \text{with } \epsilon = \frac{W}{\Delta\lambda}\frac{m_l}{m_c},$$

where θ_c, θ_l, m_l, and m_c are the position angle and degree of polarization of the continuum and of the emission lines, W is the total equivalent width of the emission lines and $\Delta\lambda$ is the width of the filter. The continuum has a higher polarization ($\sim 20\%$) than the emission lines ($\sim 1\%$–2%) and $W/\Delta\lambda \sim 0.2$, leading to an upper limit of $\Delta\theta \lesssim 1°$.

The location of the active nucleus as determined by the polarization analysis is therefore good. Moreover this method does not suffer from any ambiguity concerning the interpretation of the nature of the emission. We are only assuming that the source of reflected light is the active nucleus.

A variety of different methods of locating the position of the nucleus have been used by previous workers. Evans et al. (1991) defined the nucleus as the apex of the ionization cone observed in their emission-line images. They concluded that it is shifted towards the South with respect to the peak observed in the continuum light by Lynds et al. (1991). However, since the ionization cone morphology depends on the emission level chosen as the boundary for the cone itself (Macchetto et al. 1994), large errors are associated with this method. Braatz et al. (1993) found that the peak at 12.4 μm is 0".30 $\pm$ 0".15 away at PA 200° $\pm$ 30°, from the optical continuum peak.

Figure 13 (Plate 6) shows an FOC/COSTAR continuum image of NGC 1068 (Macchetto et al. 1994). On this image we have marked the position of the nucleus with a cross, whose size indicates the internal errors of 0".05 and the effect of the

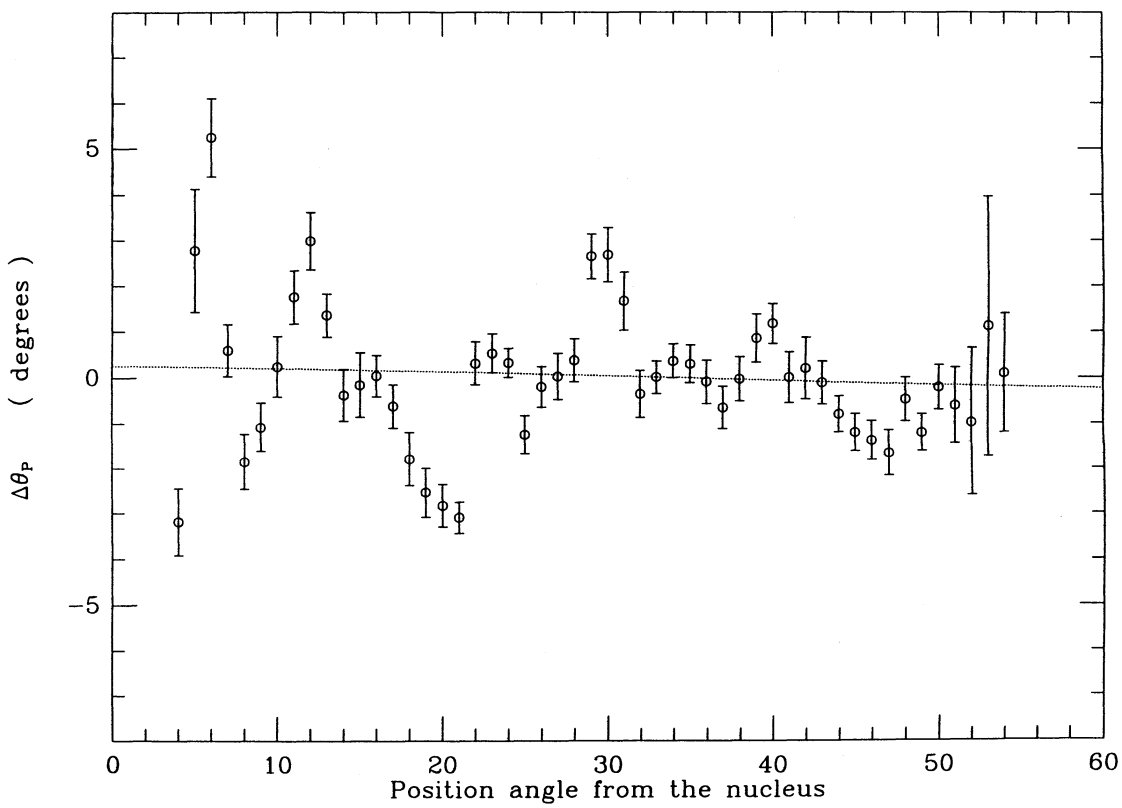

FIG. 11.—Deviations of the UV polarization vectors pattern from a perfect circular symmetry; each point shows the average deviations along a given position angle from the position of the nucleus. The dotted line shows the pattern obtained for illuminating source of $a = 0".3$ of radius.

PLATE 6

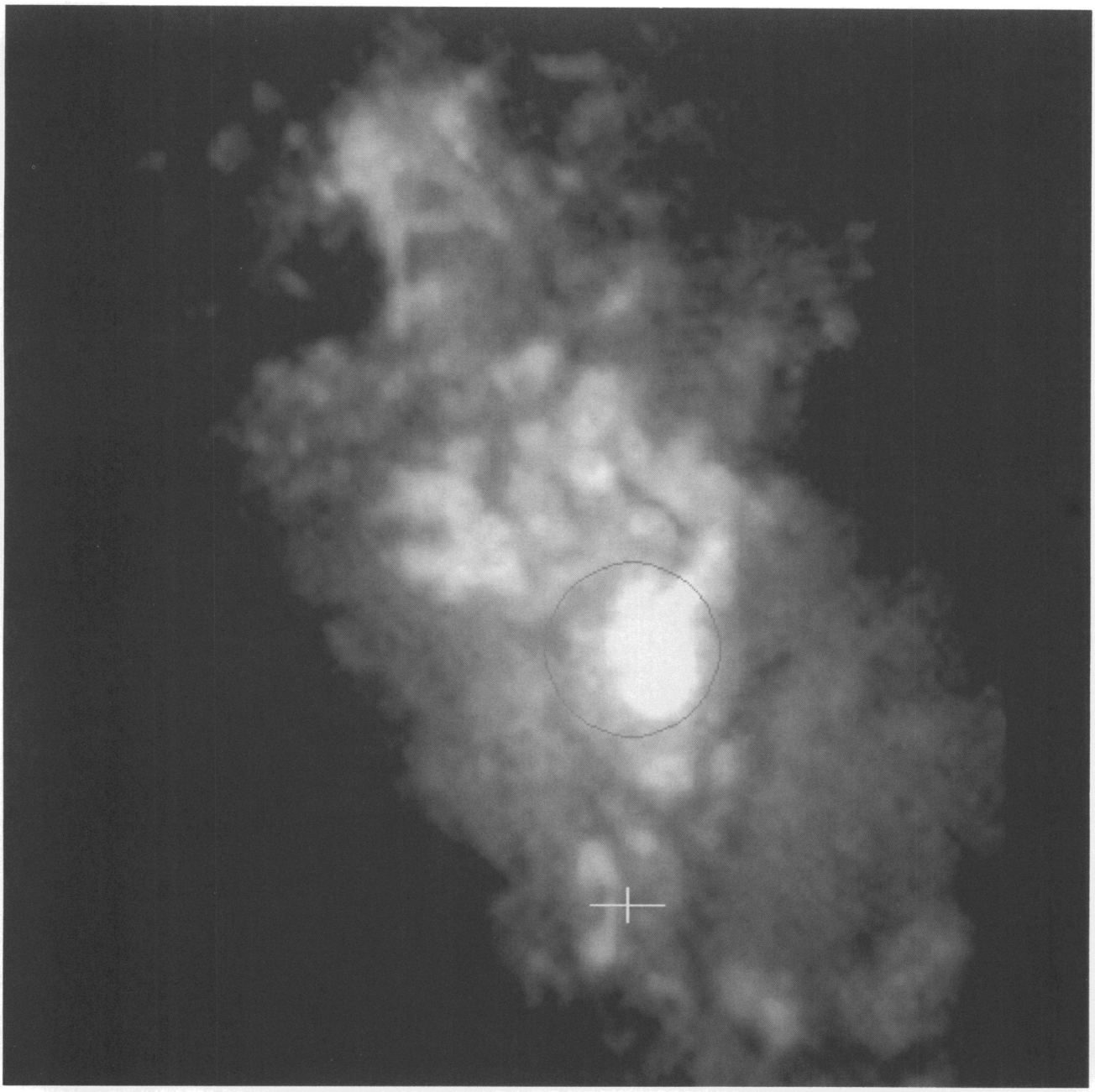

FIG. 13.—FOC/COSTAR continuum image of NGC 1068 (Maccheto et al. 1994). The field of view is 3".2 × 3".2. The position of the nucleus is marked with a cross whose size indicates internal and systematic errors. The position of the source of scattered [O III] emission is indicated with a circle and is coincident with the brightest region of oxygen emission, cloud B.

CAPETTI et al. (see 446, 160)

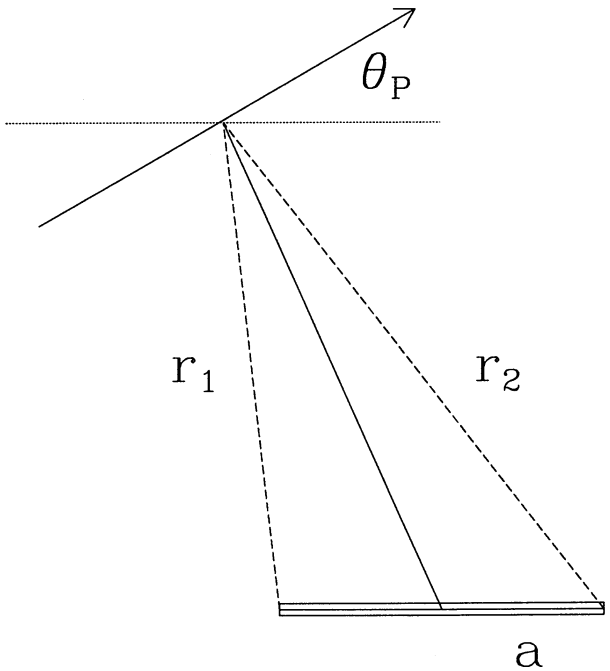

FIG. 12.—Geometric scheme used to obtain the polarization pattern of an extended illuminating source.

systematic errors. Our determination of the nominal position for the nucleus is shifted by 0".65 at PA 168° from the position of the continuum peak. This offset corresponds to ~70 pc. The nucleus is also shifted toward the southeast (0".43 at PA 146°) with respect to the IR peak and to the apex of the emission cone.

The different position of the nucleus as determined by the polarization structure and by infrared imaging indicates that the material obscuring the torus is optically thick even at 12.4 μm; this result is consistent with indications derived from X-rays (Elvis & Lawrence 1988) and CO observations (Tacconi et al. 1994) that the torus column density is $N_H \gtrsim 10^{24}$ cm^{-2}.

6. POLARIZATION PROPERTIES OF THE NUCLEAR REGION

The position of the scattered source is only 0".1 west from the pair of highly polarized clouds (see Fig. 4) and within the measurement errors it could be located between them.

In this region we find $P = 42.7\%$ in the UV and $P = 9.1\%$ in the visual. The polarization angles are similar being $\theta = 66°$ in the UV and $\theta = 69°$ in the visual; this suggests that the polarization in the visual (as well as in the UV) is dominated by continuum polarization. The polarized flux, over an area of 0".15 × 0".45, is $I_P = 5.3$ in the UV and $I_P = 8.9$ in the visual in unit of 10^{-16} erg cm^{-2} s^{-1} Å^{-1}.

Figure 13 shows that these clouds can be identified with the peculiar "twin-crescent" object in the FOC/COSTAR images of NGC 1068 (Macchetto et al. 1994). This is a ring like or double-jet like feature. It is extended about 0".4 in the north-south direction and ~0".1 in the EW direction and is oriented at PA +4°. The line and continuum emission morphologies are significantly different. The "twin-crescent" shows an excess of continuum over line emission with respect to what is typical for the rest of the NLR. Even with its excess continuum, this peculiar object is still prominent at an emission-line feature. From these higher resolution FOC/COSTAR images, it is possible to estimate the dilution due to unpolarized light from its surroundings; within the region used to estimated the polarization parameters, about 60% of the total flux is background (or foreground) emission, unrelated to the "twin-crescent," and very likely unpolarized. Therefore, the polarization level of this object, corrected for the dilution, is much higher, close to 100%! Therefore, the "twin-crescent" object is a reflection image.

Macchetto et al. (1994) suggested four alternatives for the origin of this object: (1) a disk (or torus), (2) an expanding bipolar structure, (3) an echo or reflection of light from the hidden nucleus or (4) a coincidentally located evolved SNR. The very high polarization level rules out at least two of these interpretations, (1) and (4). It suggests that emission from this object is indeed due to reflection of the light from the hidden nucleus which would lie at its center. It may be tracing the boundary of material ejecta ploughing through the ISM; the expanding material reflects the nuclear emission. Alternatively, or in addition, the enhancement in the density due to the expansion produces the enhancement of reflected light.

7. ORIGIN OF THE VISUAL POLARIZATION

The polarization structure in the visual is very complex; this is due to the presence of different polarized emission components such as the [O III] $\lambda\lambda$4959,5007 emission lines, the reflected nuclear continuum and the starlight continuum.

Comparison between the polarized flux map and the [O III] map of Macchetto et al. (1994) shows that the polarization is significant only in the regions were there is detectable [O III] emission. This correlation implies that the lines are contributing significantly to the polarized flux. Further progress in understanding the observed polarization pattern can be made by considering the results obtained from ground-based spectropolarimetry. On a scale between 2".5 and 10" the position angle measured from our images, PA ~ 150°, is in agreement with that measured on the oxygen lines by Inglis et al. (see § 3.2.2) and differs significantly from that measured for the continuum. This indicates that the large-scale polarization pattern is dominated by the [O III] polarization.

Within 2".5 from the nucleus, it is known from previous spectropolarimetric analysis of NGC 1068, that the continuum polarization angle is polarized at PA ~ +90° while the [O III] lines are polarized at PA ~ +140° (Antonucci & Miller 1985). These results suggest that the region where the polarizations vectors are oriented at PA ~ 90° (see Fig. 9) is dominated by continuum polarization while in the region where PA ~135° the emission-line polarization prevails. We have shown in § 3.2 that, through a 2".8 aperture, line and continuum emission contribute equally to the polarized emission. If our interpretation is correct, the polarized flux produced by the first component (PA +90°) must be similar to that of the second component (PA +135°). This is indeed the case.

Therefore, even though the WF/PC-I polarization images contain both optical continuum and emission-line polarization, these two component are spatially separated. The diffuse polarization is dominated by the polarized [O III] emission. In contrast, the continuum polarization dominates in a quasi-linear region starting at the location of the "hidden nucleus" determined from the UV polarization pattern, and directed along PA ≈7° which includes the pair of highly polarized blobs and the continuum peak, knot B. In this region the position angle of polarization is perpendicular to the radius

vector from the inferred location of the nucleus implying that it is the source of the scattered light. The nature of this pattern suggests that the nuclear light might be collimated.

Two arguments favour the scattering interpretation for the observed [O III] polarization. If the observed polarization is to be attributed to transmission through dust, we expect the polarized flux to follow the overall light and dust distribution. On the contrary, as we described above, the polarization traces the [O III] emission. Unless the dust follows the emission lines distribution, it can be excluded as the source of the observed polarization, indicating that polarization arises from scattering.

The profile of the polarized [O III] lines is due to the superposition of illuminating clouds with different position and velocities: this naturally explains the variation of the polarization angle along the profile of these lines. In addition, the polarization position angle is different for the various emission lines observed in the optical spectrum (Antonucci & Miller 1985) which can be explained as due to different distribution of the sources of illumination from line to line. Both effects are not easily explained in terms of dichroic transmission through dust.

Applying the same method used to find the hidden nucleus (see § 5) it is possible to determine the position of the source of scattered [O III] emission. The region dominated by the continuum polarization has been excluded. This position is indicated in Figure 13 with a circle and it is coincident with the brightest region of oxygen emission, cloud B. Unlike the source of the UV continuum, the [O III] source is not hidden and can clearly be recognized in our images. Moreover the analysis of the residuals (Fig. 14) shows deviations from a centrosymmetric structure, indicating that the scattered source is extended. The extension of cloud B, $\sim 0''.1$, is not sufficient to produce this effect (see § 5 and Fig. 11); this indicates that in some locations other NLR knots can make significant contributions as sources of scattered radiation. For example, the third weak polarized component running along the edge of the ionization cone, can be produced by reflection of the NLR clouds located farther away from the nucleus. Three dimensional modeling of the clouds distribution is needed for a better understanding of the details.

This result demonstrates that scattering is also very important for forbidden lines as already known in the case for the continuum and the permitted lines.

8. THE GEOMETRY OF THE SCATTERING MEDIUM

8.1. *Distribution of the Scattering Medium*

In the innermost region the polarized flux in the UV images outlines a conical shape, ranging from PA $-15°$ to PA $+35°$; on a larger scale, however, the polarized flux is confined between PA $-5°$ and PA $+55°$. In the visible, where our images allow us to detect polarized light up to $9''$ from the nucleus, the morphology of the polarized flux is approximately linear and positioned at PA $+45°$. Recent *HST* images (Macchetto et al. 1994) show an extended conical region which stands out for its blue color and extends from PA 0° to PA $+55°$. They interpreted this UV excess as due to reflected nuclear light, a view confirmed by our results. Moreover, the opening and position angle within the innermost region are

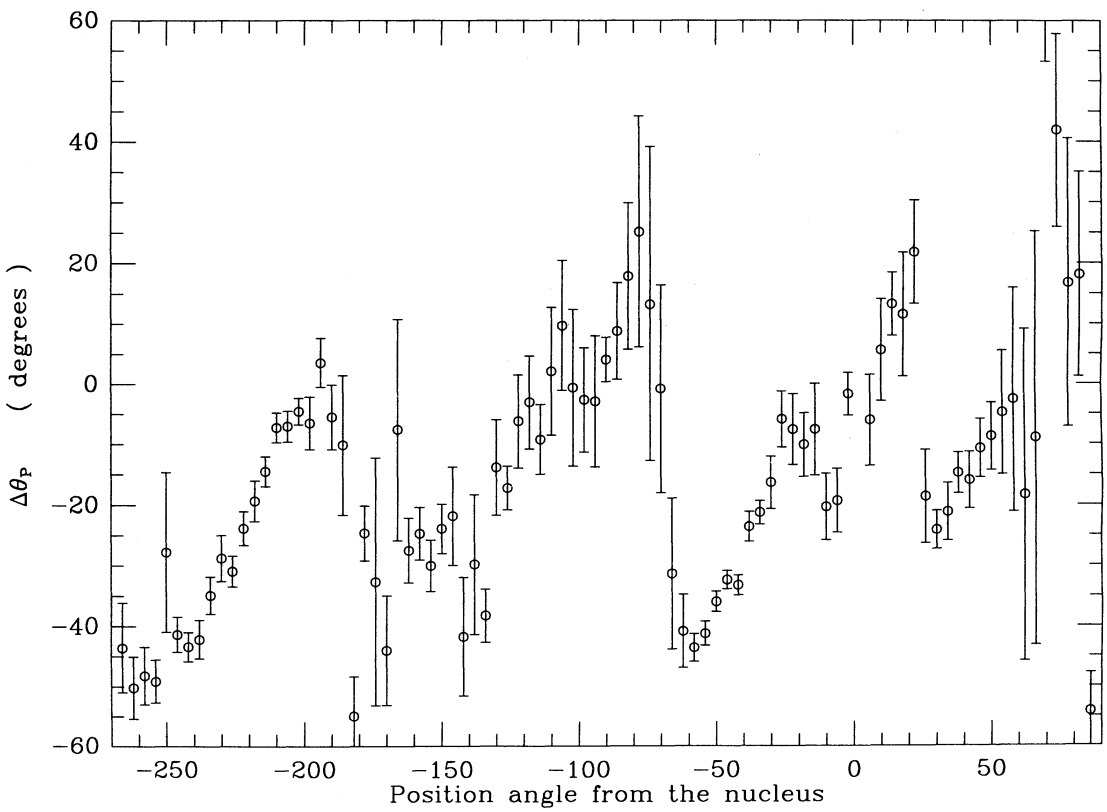

FIG. 14.—Deviations of the optical polarization vectors pattern from a perfect circular symmetry; each point shows the average deviations along a given position angle from the position of the center of symmetry.

different from those obtained on a larger scale. However they are similar to those obtained on the same region from the polarized flux, i.e., from PA $-10°$ to PA $+35°$.

Both the polarized flux and the UV excess trace the geometrical intersection between the nuclear radiation field and the distribution of the scatterers. The overall morphology is indicative of a collimated nuclear radiation field, as is already known from the appearance of the ionized gas, reinforcing the idea that the nucleus is shrouded in a dense molecular torus which allows the nuclear light to escape only along a conical region centered on its axis.

The angular extension of this conical region can be derived from the geometrical boundaries of the reflected light. However, the size and geometry of this region depend on the scale used for the measurements. This is reminiscent of the situation with the very large-scale ionized gas distributions, where Unger et al. (1992) show a sharp conical structure oriented some 30° counterclockwise from the inner cones discovered by Pogge (1988). This apparent inconsistency is solved if the nuclear light cone is not completely filled with scatterers. As we will show in the next section, the extended UV polarized flux is concentrated on the galaxy disk; moreover, the visual polarization is extended at PA $+45°$, coincident with that of the inner bar (Thronson et al. 1989) and also shows a linear morphology. We conclude that the polarized flux traces the boundaries of the gas distribution and not those of the incident light. If the cone is only partly filled, then the changing PA with distance from the nucleus is due to the different location of the gas as it streams in the inner region of NGC 1068 and intersects the cone at a changing angle. A possible geometry for the scatterers is a warped disk which would explain the different orientations and opening angle observed on different scales.

If we assume that the axis of the cone is aligned with the radio axis and the "twin-crescent" (see next section) which is PA $\sim +5°$, the cone extends symmetrically from PA $+55°$ to PA $-45°$.

We can conclude that the ionizing cone is only partly filled. Its minimum angular extent is from PA $-15°$ to PA $+55°$, corresponding to an opening angle of $\gtrsim 70°$ and is probably as large as 100°.

8.2. *The Northeast Polarized Knot*

The polarization in the northeast region is very high in our FOC observations: on average 31% but locally it reaches $\sim$60%. The total intensity map of the northeast polarized region shows a filamentary structure. The degree of polarization is higher on the filaments, and particularly on the bright arc at its west side.

The correspondence between high polarization and high brightness is not perfect, e.g., the brightest filament shows little polarization. The filaments where we detect low-polarization can be regions of enhanced line emission; as overall, the forbidden emission lines show much lower polarization, 1%–2%, than the continuum emission. However, in this case we would expect a correlation between the degree of polarization and the polarization angle pattern because the emission lines are polarized at a different position angle. This is not observed. Alternatively, the continuum emission is produced "in situ" (e.g., star-forming regions or continuum shock emission) and not reflected from the nucleus and then it is unpolarized.

Excluding these regions, the correlations between high luminosity and high polarization is very good. This is expected since where higher emission is observed, that is more polarized reflected light, the dilution of the unpolarized galaxy starlight is less important.

The observed polarization without starlight dilution is at least as high as the maximum observed polarization, that is 60% and this has an important ramification. To produce 60% polarization the average scattering angle (the angle formed by the line of sight with the line joining the NE knot to the nucleus) must be greater than $\sim 60°$. This means the NE knot cannot be at more than $\sim 30°$ from the plane of the sky. The line of nodes of NGC 1068 is at PA 55° (Walker 1968), similar to the observed PA for the NE knot, and the inclination of the disk of NGC 1068 is 39° (Burbidge, Burbidge, & Prendergast 1959). This implies that the NE polarized knot lies close to plane of the disk.

The filaments observed in the NE knot are thus mostly produced by reflected light and are tracing the distribution of the scatterers in the galaxy disk.

9. COMPARISON WITH THE RADIO OBSERVATIONS

Radio images of NGC 1068 (Wilson & Ulvestad 1983) have shown a bipolar structure extended $\sim 15''$. While the southern lobe is diffuse, the northern lobe has very sharp edges and is limb brightened, suggesting a strong interaction with the surrounding ISM. Two narrow and elongated features connect the nucleus with the lobes. The bright nuclear emission is resolved at 0.″07 resolution (Ulvestad, Neff, & Wilson 1987) in four components spanning $\sim 1''$. In recent MERLIN observations (Muxlow 1994) the southernmost component appears to have a flat spectrum as expected from a typical radio-core and it is coincident with a H_2O megamaser (Claussen & Lo 1986) which possibly indicates the position of the absorbing torus.

Unfortunately, an accurate registration (to better than 0.″5) between the radio and optical images is impossible due to the large relative astrometric uncertainties. Moreover the torus, given its very large optical depth, can be opaque even at radio wavelengths. Therefore, the radio images cannot be used as an external check for the location of the hidden nucleus.

However, the similarity between the radio and emission-line morphologies suggested to Evans et al. (1991) that these images should be registered as shown by their Figure 5, with the southernmost radio component coincident with the southernmost emission-line cloud in their images. In this case, given the position of the hidden nucleus previously discussed, the innermost $\sim$0.″5 would lack observable radio emission. Krolik & Lepp (1989) explored the structure of the obscuring torus and concluded that it is optically thick, due to free-free absorption, for $\nu \lesssim 10$ GHz. The nucleus might be obscured even at radio wavelengths. However it is unlikely that the covering factor can remain high enough to suppress the radio emission beyond a few torus scale heights and therefore the Evans et al. registration requires a real paucity of radio emission within 0.″6 of the nucleus.

The radio and optical images can also be registered by superimposing the southernmost radio component on the hidden nucleus: Figure 15 (Plate 7) presents an FOC/COSTAR continuum image of NGC 1068 from Macchetto et al. (1994) with the radio image from Muxlow (1994) overlaid, assuming this registration. In this case the region of strong radio emission lies to the east of the regions of optical emission. On the other hand, the position angle of the radio emission on sub-arcsec scale (PA $+7°$) is similar to the orientation of the "twin-crescent" object (PA $+4°$) suggesting that both are aligned with the axis of the central engine.

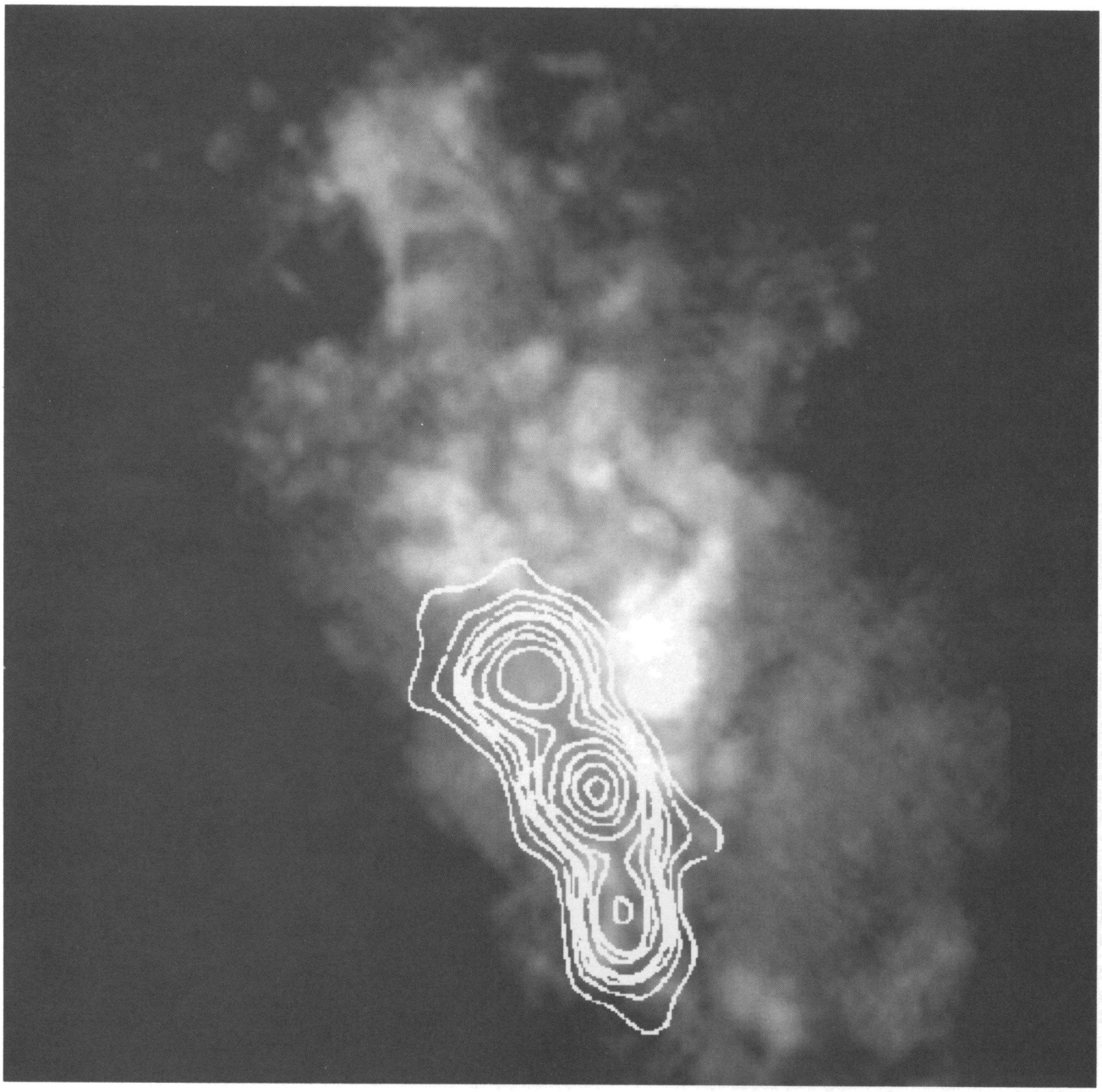

FIG. 15.—FOC/COSTAR continuum image of NGC 1068 from Macchetto et al. (1994), with superposed radio image from Muxlow (1994). The field of view is 3″.2 × 3″.2.

In either case, on the small scale the association between radio and optical emission seems unclear; in the first alternative the nucleus is either obscured or is not producing significant radio emission; in the second alternative, radio and optical emission are spatially unrelated.

On a larger scale, the situation is much clearer; the radio images show a bending similar to that observed in the optical emission and discussed in § 8: from PA +7° in the nuclear region, to PA +30° of the elongated feature, to PA ~35° of the more extended emission. There is a clear spatial correlation between the radio and polarized emission. Perhaps more interesting is the spatial coincidence between the NW sharp edge of the north lobe and the bright filament of polarized emission, where we observed $P \sim 60\%$; if the edge of the lobe is tracing the bow shock of the expanding radio plasma (Wilson & Ulvestad 1983), the filament of high polarization is likely to be related to the density enhancement of scatterers induced by the expanding lobe (Taylor, Dyson, & Axon 1992). The radio edge on the NE side does not correspond to an optical filament. The north east region seems to be deficient of gas, as derived from the distribution of polarized flux and UV excess, with respect to the northwest region. Therefore, the leading edge of the radio plasma is interacting with a lower density external medium; this medium is probably too tenuous to produce (or scatter) significant emission.

10. DISCUSSION

These *HST* observations offer a clear geometrical picture of the nuclear region of NGC 1068. The source of nuclear radiation is completely hidden to our view at all wavelengths from the infrared to the X-rays and possibly even at radio wavelengths.

However, at a distance of only ~20 pc, a "twin-crescent" structure is present. Its very high level of polarization ($P \sim 100\%$ in the UV after correction for dilution) indicates that is totally reflected light. Its morphology is probably determined by an outflow from the hidden nucleus which would lie at its center; this interpretation is also supported by the similarity of position angle with the sub-arcsec radio emission. The "twin-crescent" must lie outside the nuclear obscuring material, e.g., the torus; the vertical extension of the torus must be smaller than the inner size of this peculiar object, that is $\lesssim 20$ pc.

The brightest emission region in both continuum and line-emission, cloud B, which have been previously identified with the nucleus of NGC 1068, is in fact located at 0".65 (70 pc) north of the nucleus. This feature is saturated in our FOC images; however in the WF/PC-I images, the perpendicular to the polarization vector points to the hidden nucleus as determined by our UV observations, indicating a significant contribution from scattered nuclear light. Moreover, its color is significantly bluer than is typical for the rest of the NLR (Macchetto et al. 1994). These results are in agreement with *HST* UV spectropolarimetric observations that found $P \sim 20\%$ at PA +87° (Antonucci et al. 1994). However, there is a displacement between the continuum and emission-line peaks (0".05); the direction of the displacement also points to the hidden nucleus. Cloud B may indicate the location of a shock driven by the interaction of gas outflowing from the nucleus. Alternatively the scattering medium in cloud B is different to what is typical for the whole NLR and is preferentially scattering the short-wavelength radiation, suggesting that electron scattering is dominant in this region. Finally, the optical polarization is dominated by continuum emission in a quasi-linear region, aligned with the inner radio axis and including cloud B; this suggests that the nuclear emission can be beamed. In this case cloud B, which is colinear with the inner radio structure, may have a more direct view of the nucleus.

The nuclear radiation emerges from the nucleus confined within a cone and is reflected towards our line of sight by an extended ($\gtrsim 9''$) scattering medium. The distribution of polarized flux (i.e., of scattered light) is dominated by the distribution of scatterers inside the nuclear radiation cone which is only partly filled. Therefore only a lower limit to its angular extent can be derived, which is $\gtrsim 70°$. The scatterers are prevalently found to be aligned with the inner stellar structure, but the morphology is particularly complex. A possible geometry for the scatterers is a warped disk.

The nature of the scattering medium is not an issue that can be specifically addressed with our data; in fact no spectral information can be derived from it. However, we notice that in the UV polarization image, there is a transition between relatively low (~15%) and high (~30%) percentage of polarization that can correspond to a difference in the scattering medium. Unfortunately this effect can also be due to a different orientation of the scatterers relative to the plane of the sky which produces a different polarization level.

The nucleus is the dominant, but not unique source of scattered emission and especially in the case of forbidden-lines which are not produced in the Broad Line Region. Scattered [O III] emission pervades most of the NLR and its source is identified with the region of bright line-emission, i.e., cloud B.

This result has several interesting implications. The morphology of the NLR is distorted by this reverberated emission and many regions are "ghosts" of brighter features. Line widths and profiles can be heavily modified by bulk or thermal motion of the scatterers. Attempts to build a kinematical model of the NLR can strongly be affected by this scattered component.

As well as the [O III] emission, the continuum emission from cloud B is also being scattered: therefore multiple scattering of nuclear light is expected and can be particularly important for regions close to cloud B.

This complex physical and geometrical scenario is consistent with spectropolarimetric observations. We already discussed that the perpendicular to the polarization vector derived by Antonucci et al. (1994) on cloud B points to the hidden nucleus; they also noted an increase of the position angle with increasing size of the aperture (from PA +87° to PA +96°) which is explained by the contribution of extended scatterers oriented at larger position angles as seen from the nucleus. This effect is particularly important for the WUPPE observations (Code et al. 1993) where the NE polarized knot is included in the aperture, causing the position angle to be $\theta = 112°$.

The difference in polarization position angle of the forbidden lines with respect to the continuum is also explained because the source of illumination is different. The same argument can explain the differences in position angle from line to line (Antonucci & Miller 1985). Scattering of forbidden lines also explains the different position angle observed in the polarized profile of the [O III] as due to scattering from clouds at different location and different velocities.

The picture emerging from these results is consistent with the unified model for Seyfert galaxies. The nucleus of NGC 1068 is hidden to our view; the observed centro-symmetric

polarization pattern is very good evidence for the presence of an obscured source of emission. Due to obscuration, its emission is strongly anisotropic and emerges preferentially along the direction of the radio axis. Scattering allows us an indirect view of the nucleus through polarized light.

From these observations we also derived an upper limit to the vertical size of the obscuring torus, $\lesssim 20$ pc. This extension is largely sufficient to hide the broad line region which is argued to be present in NGC 1068.

Many of the other Seyfert galaxies imaged with *HST* show diffuse conelike morphology. Given that the majority of these also have scattered broad lines it seems highly probable that in part this conelike morphology can be due to scattering. An unfortunate consequence of this conclusion is that the overall morphology does not necessarily represent that of the intrinsically radiating material.

11. SUMMARY

We present the results of *HST* imaging polarimetry of NGC 1068 taken with the Faint Object Camera in the ultraviolet (2700–3700 Å) and the Wide Field Planetary Camera in the visual (5000–6000 Å) at a resolution of 0".06 and 0".08, respectively.

The systematic and statistical errors for the FOC observations are smaller than 1.0% for the fraction of polarization and less than 2 degrees for the position angle; this high accuracy in the polarization measurements is confirmed by the very good agreement with previous measurements both in the optical and in the ultraviolet. From the WF/PC-I data we can similarly derive accurate polarization parameters.

In the innermost regions, the UV polarization image is dominated by a small number of resolved clouds which follow closely the structure of the total intensity image with typical polarization of 8%–15%; a major exception is a pair of clouds seen 0".7 southeast of the peak of emission. They reach 50% polarization. Farther out from the nucleus the polarization is much higher, ranging from 20% up to 60%.

The structure seen in the visual polarization image is quite different from that observed in the UV images; this is expected since the filter used also includes the prominent [O III] emission lines. Extended polarized regions can be found toward the east and the southwest of the brightest regions. The pair of polarized shells is clearly detected and resolved from these observations. The polarization level is much smaller than in the FOC images, typically 3% with peak at 10% on the polarized blobs.

The polarization vectors are disposed in a circular pattern, as expected in the case of scattering from a pointlike emission source. We can accurately (within 0".05) determine the position of the nuclear source. It is shifted 0".65 south of the peak of continuum emission seen in the previous ultraviolet and optical *HST* observations. This result is not significantly affected by the exact structure of the reflected source or from the presence of polarized emission lines. The nucleus is also displaced from the peak of the mid-infrared emission indicating that the obscuring material is optically thick at this wavelength.

The position of the scattered source is only 0".1 west from the pair of highly (43%) polarized clouds (which is within the measurements error). These clouds can be identified with the peculiar "twin-crescent" object recently discovered in NGC 1068. This is a ringlike or double-jet like extended feature $\sim 0".4 \times 0".1$. The polarization level of this object, corrected for dilution, is much higher, close to 100%. Therefore, the "twin-crescent" object is a reflection image. This suggests that this object is due to reflection of the light from the true, hidden nucleus which would lie at its center. In this case it may be tracing the boundary of material ejecta ploughing through the ISM.

In the visual polarization distribution, two components oriented at different position angle can be seen. These components correspond to spatially resolved regions where either the continuum or [O III] emission line polarization dominate. They contribute equally to the polarized flux within a large 2".8 aperture. The polarized flux extends much farther toward the NE and the SW. The comparison with ground-based spectropolarimetric observations indicates that the polarization from the [O III] lines dominates these regions. The polarized flux distribution follows the [O III] emission and not the total emission as expected if the polarization is caused by dichroic transmission through dust. Polarization from scattering is then required. This mechanism also naturally explains the variation of the polarization angle along the profile of the [O III] lines and the difference in polarization position angle from line to line. The position of the source of scattered emission line is coincident with the brightest region of oxygen emission: unlike the source of the UV continuum, the [O III] source is not hidden and can clearly be recognized in our images. The analysis of the residuals shows that the scattered source is extended. Therefore, scattering is important to understand the properties of the forbidden lines as well as those of the continuum and permitted lines emission.

In the innermost region the polarized flux in the UV images outlines a conical shape, ranging from PA $-15°$ to PA $+35°$; on a larger scale, however, the polarized flux is concentrated between PA $-5°$ and PA $+55°$. To explain these results, the nuclear radiation cone has to be partly filled with scatterers; the polarized light traces the boundaries of the gas distribution and not those of the incident light. The minimum angular extent of the radiation cone is from PA $-15°$ to PA $+55°$, corresponding to an opening angle of $\gtrsim 70°$.

The polarization of the reflected featureless continuum on the northeast knot is $\lesssim 60\%$. This requires that the NE knot lies at less than 30° degrees from the plane of the sky and close the galaxy disk plane. The filaments observed in the NE knot are mostly produced by reflected light and are tracing the distribution of the scatterers in the disk of NGC 1068.

Given the relatively large astrometric uncertainties between the optical and radio images, the latter cannot be used as an external check for the location of the hidden nucleus. On the small scale, the association between radio and optical emission seems to unclear; depending on the registration chosen, the nucleus is not producing significant radio emission (or is obscured even at radio wavelengths); alternatively radio and optical emission are completely unrelated.

On a larger scale, we note the spatial coincidence between the NW edge of the North lobe and the filament of highly polarized emission; this filament is likely to be related to the enhancement of the density of the scatterers induced by the expanding radio lobe.

New *HST* observations are very important to refine many of these results. The corrected optics of the FOC will allow a detailed study of the polarization structure of NGC 1068, especially in the brighter region which are saturated in the images discussed in this paper. In particular the conjecture that there may be a collimated radiation field illuminating cloud B can be

tested. Imaging polarimetry of the forbidden lines will enable the three-dimensional distribution of emitting and scattering gas to be determined. Finally, spectropolarimetry of the "twin-crescent" will offer important constraints on the dynamics of this region: reflected light from an expanding bipolar structure shows a characteristic systematic redshift in its spectrum and a significant broadening of the lines. Moreover, given the relative closeness of the "twin-crescent," this will also offer more direct information on the hidden nucleus of NGC 1068.

From what we have learned to date for NGC 1068, *HST* imaging polarimetry in the lines and continuum of many other of the well-studied Seyferts is essential to our understanding of the inner geometry and the structure of their NLR.

We are indebted to Julian Krolik, Alan Pedlar, Stuart Young, and Pete Stockman for stimulating discussions. We would also like to thank the referee, J. Ulvestad, for his careful reading of our manuscript.

REFERENCES

Angel, J. R. P., Stockman, H. S., Woolf, N. J., Beaver, E. A., & Martin, P. G. 1976, ApJ, 206, L5
Antonucci, R. R. J. 1993, ARA&A, 31, 473
Antonucci, R. R. J., Hurt, T., & Miller, J. S. 1994, ApJ, 430, 210
Antonucci, R. R. J., & Miller, J. S. 1985, ApJ, 297, 621
Axon, D. J., Hough, J. H., Young, S. J., & Inglis, M. 1994, in Kinematics and Dynamics of Diffuse Astronomical Media, ed. J. E. Dyson (Dordrecht: Kluwer), 66
Bailey, J., Axon, D. J., Hough, J. H., Ward, M. J., McLean, I., & Heatcote, S. R. 1988, MNRAS, 234, 899
Boksenberg, A., et al. 1994, ApJ, 440, 151
Braatz, J. A., Wilson, A. S., Gezari, D. Y., Varosi, F., & Beichman, C. A. 1993, ApJ, 409, L5
Burbidge, E. M., Burbidge, G. R., & Prendergast, K. H. 1959, ApJ, 130, 26
Caganoff, S., et al. 1991, ApJ, 377, L9
Claussen, M. J., & Lo, K. Y. 1986, ApJ, 308, 592
Code, A. D., et al. 1993, ApJ, 403, L63
Elvis, M., & Lawrence, A. 1988, ApJ, 331, 161
Evans, I. N., Ford, H. C., Kinney, A. L., Antonucci, R. R. J., Armus, L., & Caganoff, S. 1991, ApJ, 369, L27
Hodge, P. 1993, Faint Object Camera Science Report 69 (Baltimore: STScI)
Inglis, M. D., Young, S., Hough, J. H., Axon, D. J., Bailey, J. A., & Ward, M. J. 1995, MNRAS, submitted
Jedrzejewski, R. 1992, Faint Object Camera Science Report 62 (Baltimore: STScI)
Krolik, J. H., & Lepp, S. 1989, ApJ, 347, 179
Krolik, J. H., & Vrtilek, J. M. 1984, ApJ, 279, 521
Lucy, L. B. 1974, AJ, 79, 745
Lynds, R., et al. 1991, ApJ, 369, L31
Maccheto, F., Capetti, A., Sparks, W. B., Axon, D. J., & Boksenberg, A. 1994, ApJ, 435, L15
MacKenty, J. W., et al. 1992, Wide Field and Planetary Camera Instrument Handbook Version 3.0 (Baltimore: STScI)
Marshall, F. E., et al. 1993, ApJ, 405, 168
McLean, I. S., Aspin, C., Heathcote, S. R., & McCaughrean, M. J. 1983, Nature, 296, 331
Miller, J. S., & Antonucci, R. J. 1983, ApJ, 271, L7
Miller, J. S., Goodrich, R. W., & Matthews, W. G. 1991, ApJ, 378, 47
Muxlow, T. W. B. 1994, in Sub-arcsecond Radio Astronomy, ed. R. J. Davis & R. S. Booth (Cambridge: Cambridge Univ. Press), 252
Paresce, F. 1992, Faint Object Camera Instrument Handbook Version 3.0 (Baltimore: STScI)
Pogge, R. W. 1988, ApJ, 328, 519
Scarrott, S. M., Draper, P. W., & Warren-Smith, R. F. 1989, MNRAS, 237, 621
Scarrott, S. M., Rolph, C. D., Wolstencroft, R. W., & Tadhunter, C. N. 1991, MNRAS, 249, 16
Schmidt, G. D., & Miller, J. S. 1985, ApJ, 290, 517
Tacconi, L. J., Genzel, R., Blietz, M., Cameron, M., Harris, A. I., & Madden, S. 1994, preprint (Max-Plank-Institut fur extraterrestrische Physik)
Taylor, D., Dyson, J. E., & Axon, D. J. 1992, MNRAS, 255, 351
Thronson, H. A., et al. 1989, ApJ, 343, 158
Turnshek, D. A., Bohlin, R. C., Williamson, R. L. II, Lupie, O. L., Koornneef, J., & Morgan, D. H. 1990, A&A, 99, 1243
Ulvestad, J. S., Neff, S. G., & Wilson, A. S. 1987, AJ, 93, 22
Unger, S. W., Lewis, J. R., Pedlar, A., & Axon, D. J. 1992, MNRAS, 258, 371
Visvanathan, N., & Oke, J. B. 1968, ApJ, 152, L165
Walker, M. F. 1968, ApJ, 151, 71
Wardle, J. F. C., & Kronberg, P. P. 1974, ApJ, 194, 249
Wilson, A. S., & Ulvestad, J. S. 1983, ApJ, 275, 8
Young, S., Hough, J. H., Axon, D. J., Bailey, J. A., & Ward, M. J. 1995, MNRAS, submitted